Heterogeneous long-range correlated deformation of semiflexible random fiber networks

H. Hatami-Marbini and R. C. Picu
Department of Mechanical, Aerospace, and Nuclear Engineering, Rensselaer Polytechnic Institute, Troy, New York 12180, USA
(Received 6 May 2009; revised manuscript received 7 August 2009; published 16 October 2009)

The deformation of dense random fiber networks is important in a variety of applications including biological and nonliving systems. In this paper it is shown that semiflexible fiber networks exhibit long-range power-law spatial correlations of the density and elastic properties. Hence, the stress and strain fields measured over finite patches of the network are characterized by similar spatial correlations. The scaling is observed over a range of scales bounded by a lower limit proportional to the segment length and an upper limit on the order of the fiber length. If the fiber bending stiffness is reduced below a threshold, correlations are lost. The issue of solving boundary value problems defined on large domains of random fiber networks is also addressed. Since the direct simulation of such systems is impractical, the network is mapped into an equivalent continuum with long-range correlated elastic moduli. A technique based on the stochastic finite element method is used to solve the resulting stochastic continuum problem. The method provides the moments of the distribution function of the solution (e.g., of the displacement field). It performs a large dimensionality reduction which is based on the scaling properties of the underlying elasticity of the material. Two examples are discussed in closure.

DOI: 10.1103/PhysRevE.80.046703 PACS number(s): 02.70.−c, 62.20.D−, 87.16.Ka, 46.65.+g

I. INTRODUCTION

Semiflexible networks are the building blocks of many biological and nonbiological structures such as tissue scaffolds, blood vessels, extracellular matrix, and battery substrates [1–4]. The cytoskeleton of eukaryotic cells, a random network of F-actin, microtubules, and intermediate filaments, is another example of such structures. The cytoskeleton controls the mechanical and transport properties of the cell, including the transport of biomolecules within the cytoplasm, cell migration, and cell chemomechanical transduction and signaling [5,6]. In semiflexible fiber networks, the persistence length, the distance along a given fiber over which orientation correlations are lost, is large. In such cases the elastic strain energy is stored in both stretching and bending deformation modes of filaments. The response of these structures to external loadings is quite different from that of flexible networks [7–10].

The mechanics of random fiber networks was studied numerically, analytically, and experimentally. In analytic models it is often assumed that the network deforms affinely [11–13]. Cox [11] computed the elastic constants of dense fiber mats in terms of their microstructure (fiber orientation) by assuming that all fibers span the entire problem domain and are only loaded at their ends. Astrom *et al.* [12] and Wu and Dzenis [13] extended the Cox model to networks of discontinuous fibers which are modeled either as Euler-Bernoulli beams, Timoshenko beams, or as simple trusses. The overall response of the network is obtained by requiring the network deformation to be locally compatible with that of the effective homogeneous continuum subjected to the same far-field loading, i.e., the affine deformation assumption. However, it is well documented that the deformation of randomly cross-linked fibers, such as that of other disordered media [14–17], is nonaffine [1,18–22], i.e., the local strain field is not homogeneous and is distinct from the far-field imposed strain. The energy level at which the actual (nonaffine) deformation occurs is lower than the energy corresponding to the affine deformation. Chandran and Barocas [1] indicated that the actual system-scale stress in random fiber networks subjected to displacement-strain boundary conditions is about three times lower than the stress predicted using the affine deformation assumption. Their results imply that in random networks there is almost no correlation between the strain in a fibril and its orientation.

The elasticity of random fiber networks was studied extensively by numerical simulations, the central goal being to understand how various microstructural parameters affect the network elastic properties. Wilhem and Frey [18] studied the elasticity of random networks consisting of rigid rods. They computed the relation between the shear modulus and the fiber density and showed that the network elasticity is dominated by bending deformation modes in the intermediate scaling regime. Heussinger and Frey [23] compared the behavior of foams and fiber networks and related their elastic properties to the microstructure. They indicated that the macroscopic shear modulus of random networks is almost independent of the fiber length. Head *et al.* [19,20] conducted a comprehensive study of random fiber networks and showed that while networks with large fiber density behave affinely, low density networks deform nonaffinely. Moreover, Head *et al.* [24] investigated numerically the response to point forces and force dipoles. These studies show that the macroscopic behavior of random networks is highly dependent on the local nonaffinity of the deformation field. A strain-based nonaffinity measure was introduced in [21,25], and it was observed that the nonaffinity exhibits a power-law dependence on the scale of observation in semiflexible networks. Other nonaffinity measures [20,22] show similar power-law scaling for the nonaffine deformation of random networks.

The mechanics of random fiber networks was also studied experimentally. The effect of cross linkers on mechanical properties of F-actin networks was studied by Gardel *et al.* [26] and Wagner *et al.* [27]. It is shown that in semiflexible networks, the network elasticity depends strongly on the cross linker densities. Moreover, by tracking embedded probe particles in F-actin networks, Liu *et al.* [22] deter-

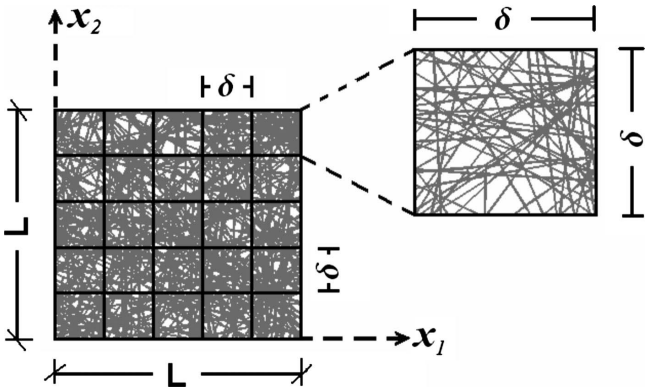

FIG. 1. Schematic representation of a random fiber network domain of size $L \times L$ probed using a regular overlay mesh of characteristic dimension δ. All fibers are of the same length, $L_0 < L$.

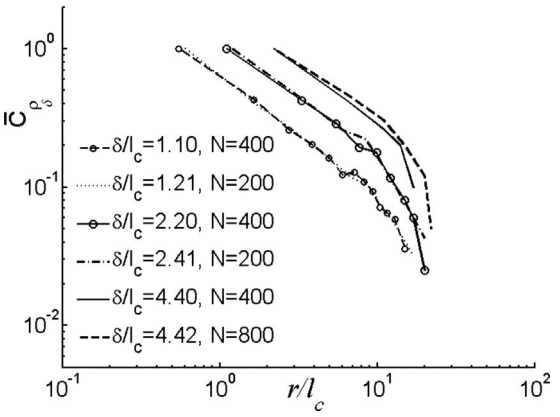

FIG. 2. Normalized autocorrelation function of the density distribution for networks with various fiber number densities probed at different length scales δ/l_c. The power-law scaling is independent of the fiber density. Note $L_0/2l_c=14$, 28, and 56 for $N=200$, 400, and 800, respectively.

mined the network microscopic deformation and reported a power-law degree of nonaffinity which depends on polymer-fiber length and cross-link density.

In this paper, we investigate first the local elasticity of semiflexible random networks by probing the fields and elastic moduli on various scales. To this end, the domain is virtually decomposed in patches of dimensions equal to the probing length and the local elasticity is evaluated based on the local stress and the deformation of the respective subdomain. It is observed that the fiber density, the moduli and the strain field exhibit power-law spatial correlations over a range of scales bounded above by the fiber length. This indicates that the network deforms in a manner similar to heterogeneous bodies with stochastic fractal distribution of moduli. This observation leads to the need to develop a method that can be used to solve boundary value problems (and perform "homogenization") defined on such materials. Due to the presence of spatial correlations and to the stochastic nature of the problem, usual system reduction methods based on scale decoupling do not apply. We propose a technique based on the stochastic finite element method (SFEM) to address this problem.

The paper is organized as follows: the model is introduced in Secs. II–IV are dedicated to the investigation of correlations and scaling properties of the networks density and elasticity, the method proposed to solve boundary value problems is discussed in Sec. V (and Appendix D), and two examples are presented in Sec. VI.

II. MODEL DESCRIPTION

Two-dimensional (2D) networks are generated by depositing straight fibers of length L_0 in a square domain of dimensions L. Fiber centers are randomly distributed in the problem domain and the fiber orientation has uniform distribution over $(0, \pi]$. The fiber number density, N, is defined as the number of fiber centers per unit area. Fibers are connected to each other rigidly at the intersection points and are modeled as homogenous elastic beams with constant Young's modulus and cross section. The dangling ends of fibers carry zero strain energy and are not considered in the model. The fiber length, L_0, the mean fiber segment length, l_c (inversely proportional to the fiber number density, N), and the system size L are the characteristic length scales of the structure. An additional length scale is $l_b = \sqrt{\kappa/\eta}$ which represents the relative importance of bending and stretching deformation; κ and η are the bending and stretching stiffness of the filaments, respectively.

The deformation of the network subjected to the far-field boundary conditions is evaluated by minimizing its potential energy. The strain energy of a fiber can be written as

$$U = \frac{1}{2}\kappa \int (\nabla^2 u)^2 ds + \frac{1}{2}\eta \int \left(\frac{dl(s)}{ds}\right)^2 ds, \tag{1}$$

where u is the transverse displacement of the fiber, s is its contour length and $dl(s)/ds$ is the axial strain. The total strain energy of the system is obtained by summing over all fibers. The solution is obtained with a finite element solver.

III. SCALING PROPERTIES OF THE FIBER DENSITY

In order to probe the microstructure of the network on various scales, let us partition the problem domain by overlaying a regular grid of square elements as shown in Fig. 1. The grid is used exclusively for probing. The element size is defined by the length δ, which is also the "probing length scale." The fiber density in each element is evaluated as the total fiber length divided by the area of the element, δ^2. By this procedure, a map of densities is obtained. The mean density over the entire map is equal to the imposed mean density ($\langle\rho\rangle \sim NL_0$) and is independent of the probing length scale. Fluctuations increase as δ decreases.

The spatial correlation of fluctuations is evaluated by computing the autocorrelation function (ACF) as

$$C_{\rho_\delta}(\mathbf{r}) = \langle \hat{\rho}_\delta(\mathbf{x}) \hat{\rho}_\delta(\mathbf{x}+\mathbf{r}) \rangle_{\mathbf{x}}, \tag{2}$$

where $\hat{\rho}_\delta = \rho_\delta - \langle\rho_\delta\rangle$ is the deviation from the mean of the density in a given element of size δ and $\langle\rho_\delta\rangle = \langle\rho\rangle$. The average is performed over multiple origins, $\mathbf{x}$. Due to the isotropy

of the network, all directions in the plane are statistically equivalent and the vectorial dependence on **r** can be replaced with the corresponding scalar dependence, $C_{\rho_\delta}(r)$. The normalized ACF is evaluated as $\bar{C}_{\rho_\delta}(r)=\langle\hat{\rho}_\delta(\mathbf{x})\hat{\rho}_\delta(\mathbf{x}+r)\rangle_\mathbf{x}/\langle\hat{\rho}_\delta(\mathbf{x})\hat{\rho}_\delta(\mathbf{x})\rangle_\mathbf{x}$. Figure 2 shows $\bar{C}_{\rho_\delta}$ for networks with different mean fiber densities probed at various length scales. The function exhibits power-law scaling over about one and a half decades and a cutoff at $\delta\sim L_0/2$; beyond this limit $\bar{C}_{\rho_\delta}$ drops to zero. The scaling $\bar{C}_{\rho_\delta}(r)\propto r^{-s_\rho}$ is independent of the mean fiber density and of the probing length scale δ, with $s_\rho=0.88\pm0.04$. As δ increases, one loses information on the smaller length scales but the large scale cutoff remains the same. A larger range of the power-law scaling is obtained for networks with large mean density (smaller l_c) since smaller elements of size δ can be used. Probing is limited to elements of size $\delta>l_c$ in order to limit the number of elements containing no fibers.

The power-law scaling of the ACF indicates that the respective function has fractal properties over the respective range of scales. The exponent s_ρ is related to the fractal box dimension D_ρ as $D_\rho=3-s_\rho/2$ [28]. For the data in Fig. 2, the fractal box dimension [29] of the density surface results $D_\rho=2.56\pm0.02$. The dimension is larger than 2, which indicates a rough surface embedded in three-dimensional (3D). A similar example is the Weierstrass function which is a function of a single variable but has adjustable fractal dimension between 1 and 2 [28]. Moreover, it is noted that Fig. 2 shows that the correlation is independent of the fiber number density when both the probing length scale and the variable of the correlation function (r) are normalized with l_c. This is the result of self-similar structure of the network and causes curves corresponding to the same δ/l_c but different N to overlap.

To understand this behavior, let us consider that one drops fibers of length L_0 $(L>L_0\gg\delta)$ at random, such that a generic element i receives $\bar{n}_\delta+\Delta n_i$ fiber centers. $\bar{n}_\delta$ is the mean number of fiber centers (i.e., $\bar{n}_\delta=N\delta^2$) and Δn_i represents the variation from the mean of the number in element i. These fibers contribute to the total fiber density in element i by $\sim(\bar{n}_\delta+\Delta n_i)\delta/\delta^2$. In addition to the fibers having their center in element i, the element is also crossed by fibers having centers in element j located at a distance r_{ij} from i, $r_{ij}<L_0/2$. The probability of a fiber centered in element j to cross element i is approximately $p(r_{ij})=1/2\pi\delta/r_{ij}$, $i\neq j$. Hence, the total number of fibers centered elsewhere and crossing element i is $\Sigma_{k=1}^{Q_i}p(r_{ik})(\bar{n}_\delta+\Delta n_k)$, where Q_i is the number of elements k for which we have $r_{ik}<L_0/2$. The total fiber density (fiber length by the element area) in element i results $\rho_i=[\bar{n}_\delta+\Delta n_i+\Sigma_{k=1}^{Q_i}p(r_{ik})(\bar{n}_\delta+\Delta n_k)]/\delta$. Considering that the number of fibers with centers in i is not correlated with the respective number in any other element j, i.e., $\langle\Delta n_i\Delta n_j\rangle=\sigma_N^2\delta_{ij}$ (δ_{ij} is the Kronecker delta function) and $\langle\Delta n_i\rangle=\langle\Delta n_j\rangle=0$, one obtains for the correlation function $C_{\rho_\delta}(r_{ij})=\sigma_N^2[1/\pi r_{ij}\delta|_{r_{ij}<L_0/2}+1/4\pi^2\Sigma_{k=1}^{Q}1/r_{ik}r_{jk}|_{r_{ij}<L_0}]$ and for the normalized ACF, $\bar{C}_{\rho_\delta}(r_{ij})=C_{\rho_\delta}(r_{ij})/\sigma_N^2$. Here Q is the number of elements k located such that $r_{ik}<L_0/2$ and $r_{jk}<L_0/2$. The first term dominates for small r_{ij} leading to a scaling of ACF as $\bar{C}_{\rho_\delta}(r)\propto r^{-1}$ in the respective limit. The ACF vanishes identically for $r>L_0$, while for $L_0/2<r<L_0$ a transition following a r^{-2} scaling is expected.

This analysis indicates that the density correlation observed here is due to the fact that fibers cover a finite spatial domain, therefore, mediating nonlocal interactions with a range proportional to their length.

It should be noted that the standard box-counting method can also be used to probe the structure of the network on the smallest scales. This type of analysis, also performed previously by Kaye [30] for the purpose of probing the porosity of fiber-based filters, is not directly related to the analysis discussed here. However, it can be used to probe length scales $\delta\ll l_c$ for which the geometry exhibits a range of fractality with box dimension approximately 1.55. The method is not applicable for larger length scales since in this case all elements contain fibers and the dimension of the embedding space $(D=2)$ is recovered.

IV. SCALING PROPERTIES OF ELASTIC MODULI

The mean fiber density $\langle\rho\rangle$ is linearly related to the stiffness at large densities [20]. Hence, it is expected that the elastic moduli computed on the scale of elements of size δ exhibit spatial correlations similar to those of the density. In order to test this conjecture and investigate the elasticity of the network at various length scales, the local moduli have to be evaluated without separating the respective patch from the network or perturbing the system configuration in any way. Therefore, after solving for the nodal displacements of the entire network subjected to the specified far-field loading (by minimizing the system potential energy), each square subdomain is considered and the points of intersection of fibers with the patch boundaries (edges) are determined. The displacements, axial forces, and bending moments at these intersection points are evaluated from the solution of the global discrete problem (forces in fibers are directly related to nodal displacements through the stiffness matrix). Therefore, the traction distribution along the perimeter of each square element of size δ and subsequently the average stress state in the respective domain are evaluated. Let us denote this method for finding field quantities on scale δ as the "*F* method" ("fitting-based method").

In order to evaluate the average strain for each element, the displacements of the element nodes (corners) must be inferred from the displacements of the fiber-element edge intersection points. To this end, least-squares fitting is performed using linear interpolation functions. Once the displacements of the element corner points are known, the local strain results by taking the derivatives of the respective (linear) displacement field. In Ref. [21], where we investigated the scaling behavior of the strain nonaffinity in random fiber networks, we used a procedure inspired by the tensometric method to compute the effective strain on scale δ from the displacements of the fiber network nodes. The "tensometric method" ("*T* method") and the *F* method described here are compared in Appendix A and are shown to be equivalent.

The elastic constants in each element are evaluated based on the local stress and strain. The resulting stress field is an equilibrium field because the underlying network is in equi-

librium. Moreover, the resulting strain field is compatible locally since linear interpolation functions are selected and globally due to the fitting procedure which insures that the deformation of neighboring elements is compatible. Thus, we can replace each square domain by an isotropic homogeneous continuum. This fitting can be performed provided that the fiber density in the respective element is sufficiently large, condition leading to a lower limit for δ, δ_0, as discussed in Appendix B. This condition insures that the elasticity of elements of size δ results approximately local and isotropic. Furthermore, as long as $L_0/l_c > 5$, the variation in the Poisson's ratio, ν, with the fiber density is small and ν remains close to the affine prediction $\upsilon = 0.5$ [20]. The only remaining parameter that fluctuates from element to element is the effective Young's modulus, E.

The elastic constants in each element can be evaluated using an alternative method (Appendix C). Let us refer to this method as the "FEM method" (finite element-based method). In this procedure, the overlay mesh is considered as a finite element mesh. The solution of this equivalent continuum to specified boundary conditions is obtained by minimizing the global potential energy while requiring that: (1) the strain energy in each element is equal to the strain energy of the underlying patch of the fiber network and (2) the displacements computed with the continuum model are closest possible to those evaluated with the discrete model (in the least-squares sense). Therefore, the unknown variables in this formulation are the mesh nodal displacements and the elastic constants in each element. As discussed in Appendix C, the two methods lead to similar local moduli and to identical Young's modulus ACFs.

It is also necessary to inquire about the moments resulting from this procedure acting along each edge of a given element. In general, although the total moment per element vanishes as mandated by the equilibrium condition for the underlying network, the moment acting on a given edge is not zero. In such cases, a micropolar formulation for the continuum has to be used instead of the local constitutive model. However, we verified that taking elements of size $\delta > \delta_0$ is a sufficient condition to eliminate the need for higher-order constitutive formulations (Appendix B).

Let us turn now to the analysis of the stiffness map. Figure 3 shows the autocorrelation function of Young's modulus, $\bar{C}_{E_\delta}(r) = \langle \hat{E}_\delta(\mathbf{x}) \hat{E}_\delta(\mathbf{x}+r) \rangle_\mathbf{x} / \langle \hat{E}_\delta(\mathbf{x}) \hat{E}_\delta(\mathbf{x}) \rangle_\mathbf{x}$ for networks of various fiber number densities probed at different length scales, δ, with $\hat{E} = E - \langle E \rangle$. A power-law results, $\bar{C}_{E_\delta}(r) \propto r^{-s_E}$, with the exponent approximately equal to that obtained for the density, $s_E = 0.92 \pm 0.06$. The fiber number density and the scale of observation δ/l_c have no influence on s_E. The resulting fractal dimension of the stiffness map is $D_E = 3 - s_E/2 = 2.54 \pm 0.03$.

The effect of the fiber bending stiffness, l_b/L_0, on the power-law scaling of the network elasticity was also studied. The details of this analysis will appear in a separate publication; however, the main conclusions are reviewed here for completeness. For $l_b/L_0 \in (10^{-4}, 10^{-1})$, the variation in the filament bending stiffness results exclusively in a vertical shift of $\bar{C}_{E_\delta}(r)$ curves in the log-log plot (Fig. 3), the scaling exponent s_E being independent of l_b/L_0. If the fiber stiffness is smaller, $l_b/L_0 < 10^{-4}$, no correlations can be evidenced. It is important to note that density correlations always exist, but they only translate into stiffness correlations for large enough l_b/L_0. If the fiber stiffness is larger, $l_b/L_0 > 10^{-1}$, the resulting bending moments on scale δ are large and the local elasticity formulation used here does not hold.

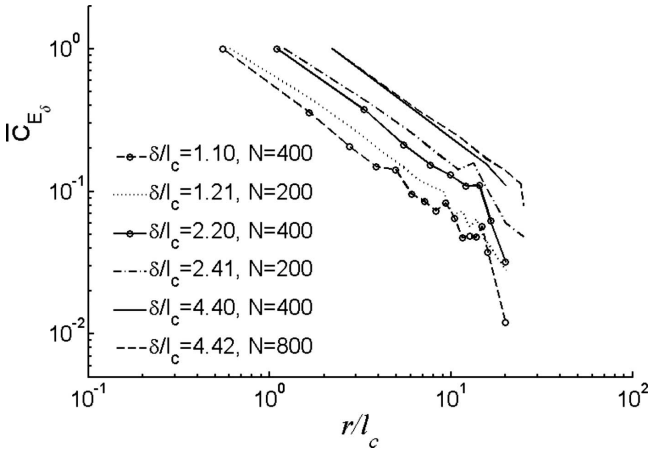

FIG. 3. Autocorrelation function of the stiffness distribution of networks with various fiber number densities probed at different length scales δ/l_c. Note $L_0/2l_c = 14$, 28, and 56 for $N = 200$, 400, and 800, respectively.

The observation that the elastic moduli are long-range power-law correlated implies that random fiber networks deform similarly to highly heterogeneous continua with stochastic fractal distribution of stiffness over a certain range of scales. In such structures, scale decoupling does not exist in the range of self-similarity and long-range correlations of all deformation fields (stress and strain) are expected. In fact, the power-law scaling of the nonaffine strain observed in random fiber networks [21] is a consequence of the scaling properties of the effective elastic constants discussed here.

In structures exhibiting long-range correlations of elastic properties and scale-free characteristics, usual methods of system reduction based on scale separation cannot be used. Therefore, a specialized method of analysis such as that developed in Ref. [31] is required. The method and its implementation are presented in the next section. The technique is most useful *in situ* in which very large semiflexible fiber network domains subjected to prescribed boundary conditions are considered. In such cases, seeking the solution by a direct approach such as the minimization of the total system potential energy is impractical, particularly if the structure is stochastic.

V. SOLUTION OF BOUNDARY VALUE PROBLEMS

A method to solve boundary value problems defined on large fiber network domains is presented in this section. Let us consider a domain Ω with prescribed, deterministic boundary conditions (on contour Γ), containing a random fiber network of fiber number density N, significantly above the percolation threshold. The structure of the network is known only in the statistical sense, i.e., the mean fiber num-

ber density and fiber orientation distribution functions are defined. Fiber elastic properties (bending and axial stiffness) and the fiber length L_0 are known and assumed identical for all fibers. The objective is to determine the solution field (e.g., displacement or strain-stress) throughout the problem domain. Since the structure is stochastic, the solution is likewise stochastic. We are interested in obtaining the first two moments of the distribution function of the solution at each point of Ω.

This problem can be approached using the SFEM developed by a number of authors and reviewed in [32]. A brief overview of the method is presented in Appendix D. In this method one seeks the minimum of the global potential energy $\Pi=\Sigma_e V^e - W$, where V^e is the strain energy of element e and W is the total work done by boundary tractions. The solution is expressed in terms of nodal displacements $\mathbf{u}(\mathbf{x},\xi)$ which are functions of position, $\mathbf{x}$, and of a random variable, ξ. The unknowns are written in a separable form as $\mathbf{u}(\mathbf{x},\xi)=\mathbf{N}(\mathbf{x})\mathbf{d}(\xi)$, i.e., a product of a deterministic function of position and a function of stochastic variables. Further, each of these functions is expanded in an orthonormal basis defined on the respective space. Specifically, $\mathbf{N}(\mathbf{x})$ is expanded in the finite element base functions (in the examples presented in Sec. VI we consider linear base functions) and $\mathbf{d}(\xi)$ is expanded as a series of chaos polynomials, $\mathbf{\Psi}(\boldsymbol{\omega}(\xi))$:

$$\mathbf{d}(\xi) = \sum_j \mathbf{c}^{(j)} \Psi_j(\boldsymbol{\omega}(\xi)). \tag{3}$$

The stochastic input to the problem is the stiffness tensor in each element, $\mathbf{D}(\mathbf{x},\xi)$ [Eq. (D3)]. When this quantity is correlated, as in the case of random fiber networks (Fig. 3), it is convenient to represent it through a Karhunen-Loeve (KL) expansion [32] as $\mathbf{D}(\mathbf{x},\boldsymbol{\xi})=\overline{\mathbf{D}}(\mathbf{x})+\Sigma_{i=1}\sqrt{\lambda_i}\omega_i(\xi)\mathbf{a}^{(i)}(\mathbf{x})$ [Eq. (D9)], where $\{\omega_i(\xi)\}$ is a set of random variables, $\{\lambda_i\}$ is a set of constants and $\{\mathbf{a}^{(i)}(\mathbf{x})\}$ is an orthonormal set of deterministic functions. The random variables $\{\omega_i(\xi)\}$ satisfy $\langle\omega_i(\xi)\rangle_\xi=0$ and $\langle\omega_i(\xi)\omega_j(\xi)\rangle_\xi=\delta_{ij}$. The constants λ and the deterministic functions $\mathbf{a}(\mathbf{x})$ are the eigenvalues and eigenfunctions of the covariance of the elastic constants, i.e., the solutions of the homogeneous Fredholm integral equation of the second kind, $\int_\Omega \mathrm{Cov}(\mathbf{x},\mathbf{y})\mathbf{a}(\mathbf{y})d\mathbf{y}=\lambda\mathbf{a}(\mathbf{x})$, where

$$\mathrm{Cov}(\mathbf{x},\mathbf{y}) = \langle \mathbf{D}(\mathbf{x},\xi)\mathbf{D}(\mathbf{y},\xi)\rangle_\xi = \int_\Omega \mathbf{D}(\mathbf{x},\xi)\mathbf{D}(\mathbf{y},\xi)dP(\xi) \tag{4}$$

and $P(\xi)$ is the probability measure defined on the domain of ξ. The eigenfunctions are orthogonal and form a complete set, i.e., $\int_\Omega \mathbf{a}^{(i)}(\mathbf{y})\mathbf{a}^{(j)}(\mathbf{y})d\mathbf{y}=\delta_{ij}$. When the variational principle corresponding to the minimization problem for Π is written in terms of these quantities (Appendix D) and when the Poisson's ratio is a deterministic quantity in each element (not necessarily identical), a system of equations for the unknown constants $\mathbf{c}$ in Eq. (3) results [Eq. (D16)]. The most important aspect of the formulation is that the system is deterministic since all stochastic components are grouped and averaged over when the balance equation is written in the weak form on the system scale. This, in turn, allows solving a single problem for all possible realizations of the random structure. Once, $\mathbf{c}$, and therefore $\mathbf{d}$ [Eq. (3)] are evaluated, the mean and variance of $\mathbf{u}(\mathbf{x},\xi)$ can be easily computed [32].

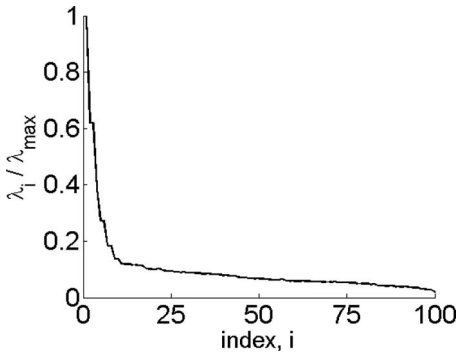

FIG. 4. Eigenvalues of the covariance matrix of the elastic constants for the network with $L_0/l_c=115$ and $l_b/L_0=0.01$ probed at $\delta/l_c=22$. The presence of few large eigenvalues guaranties the accuracy of the truncated Karhunen-Loeve decomposition.

VI. EXAMPLES

To demonstrate the capabilities of the proposed method, let us consider 2D random fiber networks without preferential fiber orientation obtained by the procedure described in Sec. II. The models are subjected to uniaxial tension. The networks (multiple realizations), probed at resolution δ/l_c, are mapped using the method outlined in the previous Sections into equivalent stochastic continua subjected to the given boundary conditions. The resulting ensemble of continua with stochastic elastic moduli is solved using the stochastic finite element method with square elements of size δ/l_c. The Poisson's ratio is identical in all elements $\nu=0.5$ [20], while Young's modulus, $E(\mathbf{x},\xi)$, is stochastic. As discussed, the autocorrelation function of $E(\mathbf{x},\xi)$ is a power law over a range bounded below by the mean fiber segment length l_c and above by $L_0/2$. Correlations on larger length scales vanish. The solution is sought at a probing length scale (resolution) $\delta/l_c=22$, arbitrarily selected within the range of self-similarity defined by $(l_c/l_c=1, \quad L_0/2l_c=57.5)$.

The covariance matrix is written based on the numerically computed autocorrelation function (Fig. 3) and making use of the isotropy of the network. Its eigenvalues and eigenvectors are computed, which allows expanding $\mathbf{D}(\xi)$ in the Karhunen-Loeve expansion.

Note that in Eq. (D9) the sum is infinite. Since a discretized version of the covariance is used, the sum includes a number of terms equal to the dimensionality of the covariance. The set of eigenvalues $\{\lambda_i\}$ is shown in Fig. 4. The number of terms in the expansion, M, which are actually kept in the formulation and used in the numerical work is a variable. Increasing M increases the accuracy of the solution but also increases the computational cost. Therefore, a tradeoff should be achieved. Usually, one includes the eigenfunctions corresponding to few largest eigenvalues. For example, with $M=4$ all eigenvalues larger than 20% of the largest eigenvalue are included in the expansion. Furthermore, a finite number of chaos polynomials are retained in the expan-

sion of the unknown solution vector of Eq. (3) [and Eq. (D14)]. n_p denotes the order of chaos polynomials. With the Karhunen-Loeve decomposition of the moduli and the expansion of the solution in terms of chaos polynomials, one follows the procedure outlined in Appendix D to find the statistics of the deformation field. In the examples considered here and some other problems in the literature [31,32], it is seen that the first two moments of the solution converge fast with respect to the number of terms in the chaos polynomials expansion and relatively slower with the number of terms in the KL expansion.

The solution obtained by this method is compared with two "reference" solutions obtained by replica averaging of (a) the equivalent stochastic continuum and (b) multiple realizations of the fiber network. In the equivalent continuum replica averaging (referred to as "*C* averaging"), the classical finite element method is used to solve a large number of realizations (~5000) of equivalent continua; each of one of these is a deterministic problem and the stiffness distribution inside the domain is obtained by sampling the probability distribution function of the stochastic Young's modulus resulting by probing the discrete model on scale δ/l_c (Sec. IV). The sampling is performed by generating correlated random variables based on the covariance matrix of the Young's modulus. The fiber network replica averaging (referred to as "*N* averaging") is based on generating and solving replicas (~250) of the fiber network. Therefore, the degree of *N* averaging is smaller then that of *C* averaging but is limited by the much larger computational expense involved. In both cases, the displacement field on scale δ/l_c is inferred and compared with the solution obtained from the stochastic finite element method at each node of the finite element mesh. It should be mentioned that *N* averaging is required to determine the correlation functions in the first place. However, a small number of replicas are required for that purpose because correlations are evaluated by considering many data pairs from each realization. Hence, correlations converge fast. In contrast, when fields corresponding to specified boundary value problem are desired, many more replicas are necessary since at each point of the problem domain one replica leads to a single data point.

Let us consider as the first example the network subjected to uniform far-field tension, $p(L,x_2)=p_0$, as shown in Fig. 5(a). Let $\mathbf{u}[i,j]$ denote the displacement vector of the node located at $x_1=(i-1)\delta$ and $x_2=(j-1)\delta$, where $i,j=1,\ldots,n+1$ and $n=L/\delta$. The nodal displacements are random variables with mean $\langle \mathbf{u}[i,j]\rangle_\xi \equiv \bar{\mathbf{u}}[i,j]$ and standard deviation $\sqrt{\langle \mathbf{u}[i,j]^2\rangle_\xi - \langle \mathbf{u}[i,j]\rangle_\xi^2} \equiv \sigma_{\mathbf{u}[i,j]}$. Moreover, let $\langle \bar{\mathbf{u}}[i,\ldots]\rangle_{x_2}$ and $\langle \sigma_{\mathbf{u}[i,.]}\rangle_{x_2}$ represent the average of the mean and standard deviation of nodal displacements along lines $x_1=(i-1)\delta$:

$$\langle \bar{\mathbf{u}}[i,\ldots]\rangle_{x_2} = \frac{1}{n+1}\sum_{j=1}^{n+1} \bar{\mathbf{u}}[i,j],$$

$$\langle \sigma_{\mathbf{u}[i,\ldots]}\rangle_{x_2} = \frac{1}{n+1}\sum_{j=1}^{n+1} \sigma_{\mathbf{u}[i,j]}. \quad (5)$$

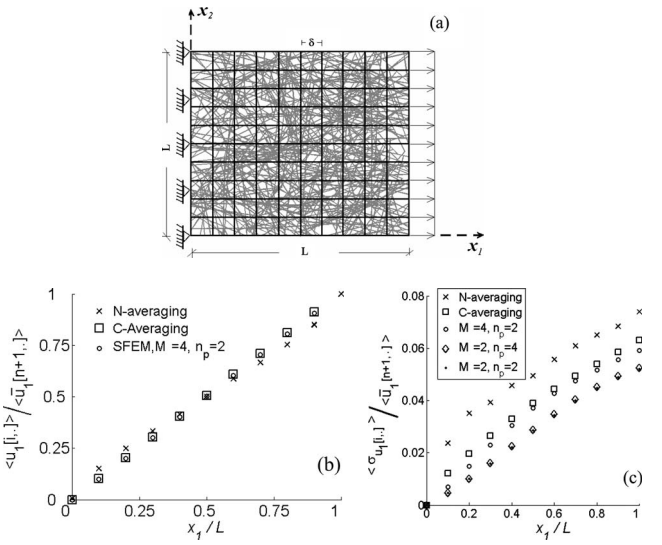

FIG. 5. (a) Schematic representation of the boundary value problem for the first example considered: a random fiber network subjected to uniform tensile loading in direction x_1. Variation in the (b) normalized mean horizontal nodal displacement, $\langle \bar{u}_1[i,\ldots]\rangle_{x_2}/\langle \bar{u}_1[n+1,\ldots]\rangle_{x_2}$ and (c) of the normalized standard deviation of the horizontal nodal displacement, $\sigma_{u_1[i,\ldots]}/\langle \bar{u}_1[n+1,\ldots]\rangle_{x_2}$, along the x_1 direction. The respective quantities are obtained by averaging along vertical lines in (a) (x_1=const). The normalization is performed with the maximum horizontal displacement at $x_1=L$. Data obtained by continuum replica averaging (*C* averaging) and network replica averaging (*N* averaging) are presented along with data from the SFEM model with various number of terms in the Karhunen-Loeve decomposition ($M=2$ and 4) and chaos polynomials of different orders ($n_p=2$ and 4).

This averaging is meaningful since, due to the symmetry of the problem, all points along any of these lines have statistically equivalent displacements. Figure 5(b) shows the normalized average of the mean horizontal displacement, $\langle \bar{u}_1[i,\ldots]\rangle_{x_2}/\langle \bar{u}_1[n+1,\ldots]\rangle_{x_2}$ as a function of $x_1=(i-1)\delta$, along with results from replica averaging. All three methods lead to consistent results.

Figure 5(c) shows the normalized average of the standard deviation of the horizontal displacement, $\sigma_{u_1[i,\ldots]}/\langle \bar{u}_1[n+1,\ldots]\rangle_{x_2}$ versus position along the horizontal line $x_1=(i-1)\delta$. Several solutions obtained with SFEM by considering various numbers of terms in the Karhunen-Loeve expansion as well as various number of terms in the expansion of the solution in chaos polynomials [Eq. (D14)] are presented. As in [31], it is observed that the number *M* of terms considered in the Kahunen-Loeve decomposition is more important in defining the accuracy of the results than the order n_p of chaos polynomials considered in the expansion of **d**. It is also noted that since a limited number of replicas have been used in the *N* averaging process, the standard deviation is overpredicted. The *N* and *C* averaging results are expected to come together if sufficient replicas are considered.

In the second example, the same structure is subjected to nonuniform far-field loading. A sinusoidal distributed force $p(L,x_2)=p_0 \sin(\pi x_2/L)$ is applied [Fig. 6(a)] in order to determine the effect of field gradients on the accuracy of the

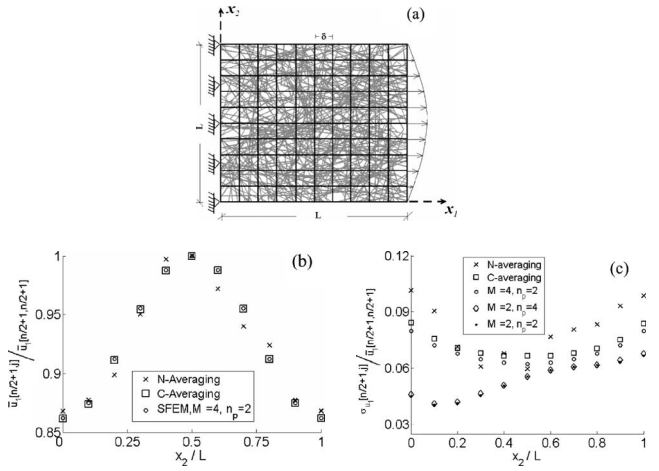

FIG. 6. (a) Schematic representation of the second boundary value problem considered: a random fiber network subjected to nonuniform uniaxial tension $p(x_2)=p_0 \sin(\pi x_2/L)$ applied at $x_1=L$. Variation in the (b) normalized mean horizontal nodal displacement, $\bar{u}_1[n/2+1,j]/\bar{u}_1[n/2+1,n/2+1]$, and (c) of the normalized standard deviation of the horizontal nodal displacement, $\sigma_{u_1[n/2+1,j]}/\bar{u}_1[n/2+1,n/2+1]$, along the vertical line $x_1=L/2$. The normalization is performed with the maximum horizontal displacement at $x_1=x_2=L/2$. Data obtained by continuum replica averaging (C averaging) and network replica averaging (N averaging) are presented along with data from the SFEM model with various number of terms in the Karhunen-Loeve decomposition ($M=2$ and 4) and chaos polynomials of different orders ($n_p=2$ and 4).

solution. The notation defined above is also used for this example. Hence, $\bar{u}_1[n/2+1,j]$ and $\sigma_{u_1[n/2+1,j]}$, where $j=1,\ldots,n+1$, denote the mean and standard deviation of the horizontal components of the displacement along the vertical line $x_1=L/2$. Moreover, $\bar{u}_1[n/2+1,n/2+1]$ represents the mean displacement of the node at $(x_1=L/2,x_2=L/2)$. Figure 6(b) shows the normalized mean horizontal displacement, $\bar{u}_1[n/2+1,j]/\bar{u}_1[n/2+1,n/2+1]$. It is observed that the mean of the deformation field predicted by the stochastic finite element method agrees with the mean displacement obtained from replica averaging over many realizations (both C averaging and N averaging).

The normalized standard deviation of the horizontal displacement, $\sigma_{u_1[n/2+1,j]}/\bar{u}_1[n/2+1,n/2+1]$ along line $x_1=L/2$ is shown in Fig. 6(c). In this case, fluctuations of the displacement field about its mean are larger than those in the case of the uniform far-field loading. As above, taking more terms in the Karhunen-Loeve expansion (larger M) improves the accuracy. The comparison with the C averaging result is positive, while the N averaging leads to an overprediction of the standard deviation due to the limited number of replicas considered.

VII. CONCLUSIONS

The elasticity of 2D semiflexible fiber networks is investigated in this work with focus on (a) the scaling of density, elastic moduli and elastic fields fluctuations, and (b) on the constitutive representation of the continuum equivalent of such discrete systems. It is shown that the fiber density and all elastic quantities investigated (including the nonaffine strains) exhibit long-range correlations and increasing fluctuations as the scale of observation decreases. This originates from the similar behavior of the density which, in turn, is determined by the fact that fibers with relatively large persistence length span a finite domain mediating nonlocal interactions between neighboring regions of the network.

The adequacy of considering a local isotropic model for the network was investigated, and it was concluded that the approximation holds as long as the probing length scale (resolution) is larger than a threshold on the order of (but larger than) the mean segment length l_c. This condition is also sufficient to ensure that the local version of elasticity can be used on the respective scales and higher-order models are not required.

The fact that the equivalent continuum map of the random network is characterized by power-law spatial correlations implies that no scale decoupling exists in the range of scales over which self-similarity is observed. Homogenization and the solution of boundary value problems defined on such domains cannot be performed using standard system reduction (multiscale) techniques. A procedure based on the stochastic finite elements method is proposed and several examples are given to demonstrate its effectiveness. The method is much faster than replica averaging and is expected to be most useful in applications requiring the solution of boundary value problems defined on very large fiber networks with stiff, long fibers in presence of uncertainty.

The method discussed here is particularly useful *in situ* in which the scale of interest (the desired resolution) is smaller than the fiber length and when $l_c \ll L_0$ (dense networks of relatively long fibers), case in which a significant scaling range exists. An example of such system is the cytoskeleton of eukaryotic cells which is a composite fiber network containing F-actin fibers and microtubules. The microtubules are stiff and span the entire problem domain. Hence all scales of interest are smaller than the upper limit of the expected scaling range. When L_0 is small and/or the scale of interest is much larger than the fiber length, no spatial correlations are present and the system can be homogenization using classical homogenization methods.

APPENDIX A: COMPARISON OF METHODS USED TO INFER LOCAL STRAINS FROM NETWORK NODAL DISPLACEMENTS

An additional consistency check is required relative to the evaluation of the effective (mean) strain on scale δ. In Ref. [21] a procedure inspired by the tensometric method was used to compute the effective strain on scale δ from the displacements of the network nodes. In this method (denoted here as the T method), the strain is evaluated by selecting three points of the network at which displacements are known. Theses points should form an approximately equilateral triangle. The probing length scale δ is taken equal to the square root of the area of the triangle. As in tensometry, the strain is computed directly from the geometry and the relative displacements of the triangle vertices. To test the consis-

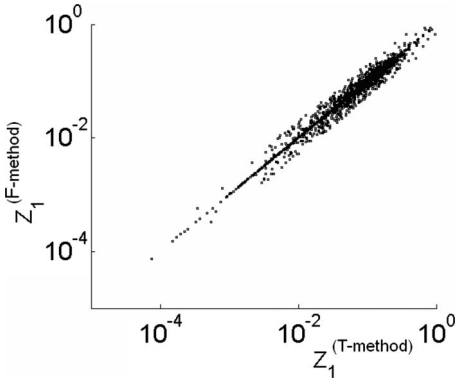

FIG. 7. Nonaffine strain variance computed with the method discussed in Sec. IV, $Z_1^{F\ \text{method}}$, and that used in Ref. [21], $Z_1^{T\ \text{method}}$, for a network of density $N=400$ fibers per unit area probed on scale $\delta/l_c=2.28$.

tency between the results presented in [21] and those discussed here, let Z_1 denote the variance of the nonaffine strain (normal strain in the loading direction):

$$Z_1 = \left(1 - \frac{\varepsilon_{11}}{\varepsilon_{11}^{aff}}\right)^2. \tag{A1}$$

Figure 7 shows Z_1 evaluated with the method discussed in the main text (F method) and with that used in Ref. [21] (T method) for a network of density $N=400$ fibers per unit area probed at length scale $\delta/l_c=2.28$ and subjected to uniform uniaxial tension in the x_1 direction (Fig. 1). The two methods predict the same level of nonaffine strain fluctuations. We performed this comparison at various probing length scales and for networks of different fiber densities and similar behavior is observed in all cases.

APPENDIX B: THE ISOTROPY ASSUMPTION AND THE MICROPOLARITY OF THE HOMOGENIZED EQUIVALENT CONTINUUM

Replacing the discrete material with "an equivalent" continuum rises questions regarding the nature of the constitutive model to be used. At large length scales (large δ), the homogenized continuum is expected to be isotropic. However, as δ decreases, anisotropy becomes important. The anisotropy is related, for example, to local fluctuations of fiber orientation in the given subdomain. Furthermore, although the element must be in equilibrium, the moments acting along each of its edges may not vanish. In this case the usual local formulation of elasticity must be replaced with a micropolar version. Therefore, determining the scale δ at which a local isotropic assumption becomes acceptable is important.

Let us consider first the issue of anisotropy. If c_{11}, c_{12}, c_{66} denote the elastic constants of a homogenous continuum with cubic symmetry, the degree of anisotropy may be represented by the parameter [33]

$$A = \frac{c_{11} - c_{12}}{2c_{66}}. \tag{B1}$$

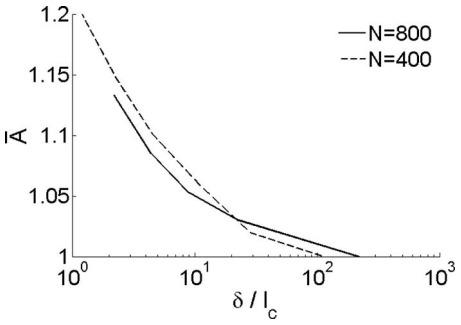

FIG. 8. Average degree of anisotropy, $\bar{A}$, of equivalent homogeneous continuum versus the probing length scale, δ/l_c, for systems with $N=400$ and 800 fibers per unit area and $l_b/L_0=0.01$.

Let $\bar{A}$ denote the average of this dimensionless quantity over all elements of size δ/l_c. Figure 8 shows $\bar{A}$ as a function of the probing length scale for networks with $N=400$ and 800 fibers per unit area and $l_b/L_0=0.01$. It is seen that the approximation made by modeling the elasticity of patches of size δ/l_c with a homogenous isotropic elastic model improves as δ increases, the error is always smaller than 20% as long as $\delta/l_c>1$. For $\delta/l_c=22$ used in the numerical examples of Sec. VI, the error is negligible.

To investigate the degree of micropolarity, it is necessary to evaluate the moments resulting from the action of axial forces and bending moments in each fiber that intersects a given element edge. To use a local form of elasticity for the equivalent continuum, the sum of these moments along each element edge must be relatively small. To quantify their magnitude, the dimensionless quantity,

$$B = \frac{S_M}{S_F \delta}, \tag{B2}$$

is computed, where S_F and S_M are the absolute values of the force and bending moment acting along given element edge of size δ/l_c, respectively. The average of B, $\bar{B}$ for networks with $N=400$ and 800 fibers per unit area and $l_b/L_0=0.01$ is shown in Fig. 9 as a function of the probing length scale δ/l_c. It is observed that the error associated with $\bar{B}$ is smaller

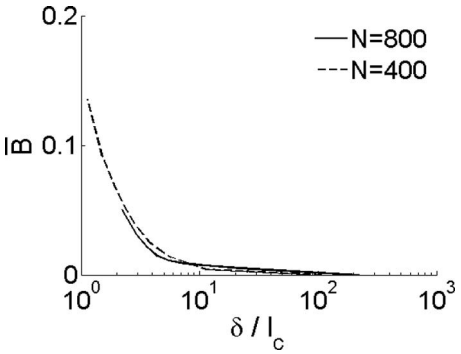

FIG. 9. Average of the dimensionless measure of the degree of micropolarity, $\bar{B}$, of equivalent homogeneous continuum versus the normalized probing length scale, δ/l_c for systems with $N=400$ and 800 fibers per unit area and $l_b/L_0=0.01$.

than that for $\bar{A}$ at the same δ/l_c, which indicates that the probing length scale can be selected exclusively based on the tolerance imposed for the departure from isotropy.

APPENDIX C: ALTERNATIVE APPROACH TO EVALUATE THE ELASTICITY OF THE HOMOGENEOUS CONTINUUM

An alternative method (FEM method) for finding the elastic constants in each element of size δ/l_c is discussed in this Appendix. In this method, the entire overlay mesh is considered as a finite element mesh which is subjected to the same boundary conditions as the actual network. The elastic constants of each finite element and its nodal displacements are considered unknown.

Let $\mathbf{u}_k^{FE}$ be the unknown nodal displacements of the continuum mesh. The displacement at the location of network nodes, $\mathbf{x}^{(i)}$, can be expressed in terms of $\mathbf{u}_k^{FE}$ as

$$\mathbf{u}^{\mathrm{Cont}}(\mathbf{x}^{(i)}) = \sum_{k=1}^{N_{node}^{FE}} \mathbf{N}_k(\mathbf{x}^{(i)})\mathbf{u}_k^{FE}. \tag{C1}$$

$\mathbf{N}_k(\mathbf{x}^{(i)})$ represents the interpolation function corresponding to node k of the mesh evaluated at the location of the ith network node, and the sum is performed over all N_{node}^{FE} nodes of the FE model. The unknown FE nodal displacements, $\mathbf{u}_k^{FE}$, are obtained by minimizing the norm of the difference between the actual displacements $\mathbf{u}(\mathbf{x}^{(i)})$ of the network nodes and their corresponding FE estimates $\mathbf{u}^{\mathrm{Cont}}(\mathbf{x}^{(i)})$, subjected to the constraint that the continuum elastic strain energy of each square element l, U_l^{Cont}, is equal to the corresponding discrete strain energy U_l, which is the sum of the strain energy of all fibers in the domain covered by element l. Once the nodal displacements $\mathbf{u}_k^{FE}$ have been obtained (and therefore the strain), the Young's modulus of each element results simply from the respective energy U_l^{Cont}.

Figure 10 demonstrates the equivalence of this method and that described in the main text, Sec. IV (F method). It shows the PDF of the ratio between the Young's modulus computed with the two methods element by element ($E^{F\ meth}/E^{\mathrm{FEM}\ meth}$), for a network with $N=400$ fibers per unit area probed on scale $\delta/l_c=4.56$. The distribution is narrow and centered on 1. Likewise, the ACF function $\bar{C}_{E_\delta}(r)$ computed with the two sets of moduli, found with the F method and with the FEM method, are identical (inset to Fig. 10).

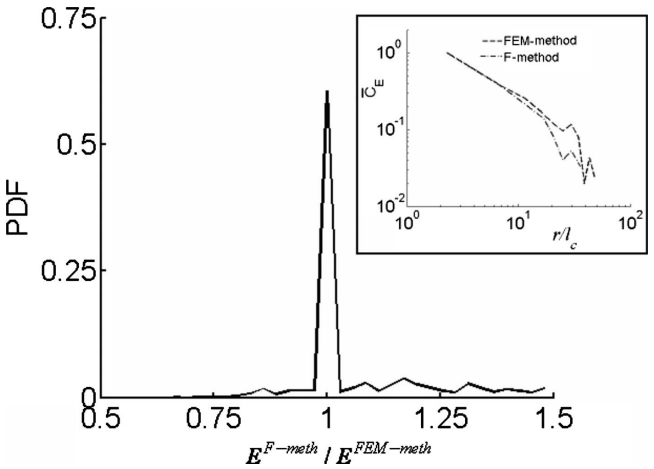

FIG. 10. Probability distribution function of the ratio of element Young's modulus $E^{F\ meth}/E^{\mathrm{FEM}\ meth}$ computed with the fitting method described in Sec. IV and with the FEM-based method described in Appendix C for a network with $N=400$ fibers per unit area probed on scale $\delta/l_c=4.56$. The inset shows the autocorrelation function of the Young's modulus evaluated using moduli determined by the FEM method for the same network. The two sets of data are spatially correlated in a similar way.

APPENDIX D: OVERVIEW OF THE STOCHASTIC FINITE ELEMENT METHOD

The Stochastic Finite Element formulation is reviewed in this Appendix. For a comprehensive overview of the methodology, the reader is referred to the book of Ghanem and Spanos [32]. Let us consider a two-dimensional domain discretized into finite elements having the elastic constants in each element described by a stochastic variable. The strain energy U^e stored in each element of area A^e can be expressed as

$$U^e = \frac{1}{2}\int_{A^e} \boldsymbol{\sigma}(\mathbf{x},\xi)^T\boldsymbol{\varepsilon}(\mathbf{x},\xi)dA^e. \tag{D1}$$

Here, $\boldsymbol{\sigma}(\mathbf{x},\xi)=(\sigma_{11}\ \sigma_{22}\ \sigma_{12})^T$ and $\boldsymbol{\varepsilon}(\mathbf{x},\xi)=(\varepsilon_{11}\ \varepsilon_{22}\ 2\varepsilon_{12})^T$ are the 2D stress and strain vectors, respectively, which are related through

$$\boldsymbol{\sigma}(\mathbf{x},\xi) = \mathbf{D}(\mathbf{x},\xi)\boldsymbol{\varepsilon}(\mathbf{x},\xi), \tag{D2}$$

where

$$\mathbf{D}(\mathbf{x},\xi) = \frac{E(\mathbf{x},\xi)}{1-v^2}\begin{pmatrix} 1 & v & 0 \\ v & 1 & 0 \\ 0 & 0 & (1-v)/2 \end{pmatrix} \tag{D3}$$

is the stiffness matrix. For simplicity and compatibility with the case discussed in the main text, we choose the Poisson's ratio v to be a deterministic variable (e.g., a constant) and the Young's modulus $E(\mathbf{x},\xi)$ to depend on position (a deterministic variable) $\mathbf{x}$ and a stochastic variable, ξ. The strain tensor is related to the displacement field, $\mathbf{u}(\mathbf{x},\xi)$ through the relation

$$\boldsymbol{\varepsilon}(\mathbf{x},\xi) = \begin{pmatrix} \partial/\partial x & 0 \\ 0 & \partial/\partial y \\ \partial/\partial y & \partial/\partial x \end{pmatrix}\mathbf{u}(\mathbf{x},\xi) = \mathbf{H}\mathbf{u}(\mathbf{x},\xi). \tag{D4}$$

and the 2D displacement field can be expressed in terms of the two-dimensional deterministic finite element shape functions $\mathbf{N}(\mathbf{x})$ and unknown nodal displacements $\mathbf{d}(\xi)$ as

$$\mathbf{u}(\mathbf{x},\xi) = \mathbf{N}(\mathbf{x})\mathbf{d}(\xi). \tag{D5}$$

It is noted that the dependence of all fields on the stochastic variable ξ follows from their dependence on the stiffness tensor which is the input stochastic quantity of the problem.

Let us consider that traction-imposed boundary conditions are specified deterministically, in the form of tractions $\mathbf{T}(\mathbf{x})$. The work performed is then written as

$$W = \sum_{eb} W^{eb} = \sum_{eb} \int_{\Gamma^{eb}} \mathbf{T}(\mathbf{x})\mathbf{u}(\mathbf{x},\xi)d\Gamma^{eb}, \tag{D6}$$

where Γ^{eb} denotes the portion of the problem domain boundary Γ corresponding to the boundary element "*eb*." Minimizing the potential energy, $\Pi = \Sigma_e U^e - W$, with respect to the nodal displacements yields the system of equations,

$$\mathbf{Kd} = \mathbf{f}, \tag{D7}$$

where

$$\mathbf{K} = \sum_e \int_{A^e} \mathbf{B}(\mathbf{x})^T \mathbf{D}(\mathbf{x},\boldsymbol{\xi})\mathbf{B}(\mathbf{x})dA^e,$$

$$\mathbf{B}(\mathbf{x}) = \mathbf{HN}(\mathbf{x}),$$

$$\mathbf{f} = \sum_e \int_{\Gamma^e} \mathbf{N}(\mathbf{x})^T \mathbf{T}(\mathbf{x})d\Gamma^e. \tag{D8}$$

The Karhunen-Loeve decomposition of $\mathbf{D}(\mathbf{x},\boldsymbol{\xi})$ is written as

$$\mathbf{D}(\mathbf{x},\boldsymbol{\xi}) = \overline{\mathbf{D}}(\mathbf{x}) + \sum_{i=1} \sqrt{\lambda_i}\omega_i(\xi)\mathbf{a}^{(i)}(\mathbf{x}). \tag{D9}$$

Substituting Eq. (D9) into Eq. (D8), one obtains

$$\sum_{i=0} \sqrt{\lambda_i}\omega_i(\xi)\mathbf{K}^{(i)}\mathbf{d} = \mathbf{f}, \tag{D10}$$

where

$$\mathbf{K}^{(i)} = \begin{cases} \sum_e \int_{A^e} \mathbf{B}(\mathbf{x})^T \mathbf{a}^{(i)}(\mathbf{x})\mathbf{B}(\mathbf{x})dA^e, & i \neq 0 \\ \sum_e \int_{A^e} \overline{\mathbf{D}}(\mathbf{x})\mathbf{B}(\mathbf{x})^T \mathbf{B}(\mathbf{x})dA^e, & i = 0, \end{cases} \tag{D11}$$

and $\omega_0(\xi) = \lambda_0 = 1$. Equation (D10) can be rewritten as

$$\left[\mathbf{I} + \sum_{i=1} \sqrt{\lambda_i}\omega_i(\xi)\mathbf{Q}^{(i)}\right]\mathbf{d} = \mathbf{g}, \tag{D12}$$

where

$$\mathbf{Q}^{(i)} = \mathbf{K}^{(0)^{-1}}\mathbf{K}^{(i)},$$

$$\mathbf{g} = \mathbf{K}^{(0)^{-1}}\mathbf{f}. \tag{D13}$$

The vector of unknowns $\mathbf{d}$ is sought in the form of a series of orthonormal chaos polynomials $\Psi_j[\boldsymbol{\omega}(\xi)]$ [32]:

$$\mathbf{d} = \sum_j \mathbf{c}^{(j)}\Psi_j[\boldsymbol{\omega}(\xi)]. \tag{D14}$$

A complete discussion of chaos polynomials is given in [32]. For example,

$$\Psi_1 = 1, \quad \Psi_2 = \omega_1, \quad \Psi_3 = \omega_1^2 - 1, \quad \Psi_4 = \omega_1^3 - 3\omega_1 \tag{D15a}$$

are among one-dimensional chaos polynomials and

$$\Psi_1 = 1, \quad \Psi_2 = \omega_1, \quad \Psi_3 = \omega_2, \quad \Psi_4 = \omega_1^2 - 1,$$

$$\Psi_5 = \omega_1\omega_2, \quad \Psi_6 = \omega_2^2 - 1 \tag{D15b}$$

are some two-dimensional chaos polynomials.

Substituting Eq. (D14) into Eq. (D12) and forming the inner product of the result with $\Psi_j[\boldsymbol{\omega}(\xi)]$ yields

$$\mathbf{c}^{(m)} + \sum_j \sum_i \varsigma_{ijm}\mathbf{Q}^{(i)}\mathbf{c}^{(j)} = \langle \mathbf{g}\Psi_m[\boldsymbol{\omega}(\xi)]\rangle_\xi, \tag{D16}$$

where

$$\varsigma_{ijm} = \langle \omega_i\Psi_j(\boldsymbol{\omega})\Psi_m(\boldsymbol{\omega})\rangle_\xi. \tag{D17}$$

The right-hand side and the quantity ς can be computed in closed form, and hence Eq. (D16) is a deterministic system of equations for $\mathbf{c}$. Its solution, together with Eq. (D14), provides the stochastic displacement field which can be used to derive the first two moments of the solution field throughout the problem domain. It should be mentioned that, in addition to the factors affecting the accuracy of the deterministic FEM solutions, the accuracy of the SFEM solution depends on the order of chaos polynomials and the number of terms used in KL decomposition of the problem stiffness matrix (Figs. 5 and 6).

[1] P. L. Chandran and V. H. Barocas, J. Biomech. Eng. **128**, 259 (2006).
[2] A. Zoumi *et al.*, Biophys. J. **87**, 2778 (2004).
[3] C. Wang *et al.*, ASME J. Eng. Mater. Technol. **121**, 503 (1999).
[4] A. Zoumi, A. Yeh, and B. J. Tromberg, Proc. Natl. Acad. Sci. U.S.A. **99**, 11014 (2002).
[5] H. Lodish *et al.*, *Molecular Cell Biology* (Freeman, New York, 2000).
[6] T. P. Stossel, Sci. Am. **271**, 54 (1994).
[7] O. Chaudhuri, S. H. Parekh, and D. A. Fletcher, Nature (London) **445**, 295 (2007).
[8] P. A. Janmey *et al.*, Nature Mater. **6**, 48 (2007).
[9] C. Storm *et al.*, Nature (London) **435**, 191 (2005).
[10] F. C. Mackintosh, J. Kas, and P. A. Janmey, Phys. Rev. Lett. **75**, 4425 (1995).
[11] H. L. Cox, Br. J. Appl. Phys. **3**, 72 (1952).
[12] J. A. Astrom *et al.*, Phys. Rev. E **61**, 5550 (2000).
[13] X. F. Wu and Y. A. Dzenis, J. Appl. Phys. **98**, 093501 (2005).
[14] F. Leonforte *et al.*, Phys. Rev. B **70**, 014203 (2004).
[15] A. Tanguy *et al.*, Phys. Rev. B **66**, 174205 (2002).
[16] H. M. Jaeger, S. R. Nagel, and R. P. Behringer, Rev. Mod.

Phys. **68**, 1259 (1996).
[17] H. Hatami-Marbini and R. C. Picu, Eur. J. Mech. A/Solids **28**, 305 (2009).
[18] J. Wilhelm and E. Frey, Phys. Rev. Lett. **91**, 108103 (2003).
[19] D. A. Head, A. J. Levine, and F. C. MacKintosh, Phys. Rev. Lett. **91**, 108102 (2003).
[20] D. A. Head, A. J. Levine, and F. C. MacKintosh, Phys. Rev. E **68**, 061907 (2003).
[21] H. Hatami-Marbini and R. C. Picu, Phys. Rev. E **77**, 062103 (2008).
[22] J. Liu *et al.*, Phys. Rev. Lett. **98**, 198304 (2007).
[23] C. Heussinger and E. Frey, Phys. Rev. Lett. **96**, 017802 (2006).
[24] D. A. Head, A. J. Levine, and F. C. MacKintosh, Phys. Rev. E **72**, 061914 (2005).
[25] H. Hatami-Marbini and R. C. Picu, Acta Mech. **205**, 77 (2009).
[26] M. L. Gardel *et al.*, Science **304**, 1301 (2004).
[27] B. Wagner *et al.*, Proc. Natl. Acad. Sci. U.S.A. **103**, 13974 (2006).
[28] K. Falconer, *Fractal Geometry: Mathematical Foundations and Applications* (Wiley & Sons, New York, 1990).
[29] In the "box-counting" method, one considers the object embedded in the n-dimensional space and plots the number of n-dimensional cubes of side δ required to cover the entire object versus δ. If the object has fractal scaling properties, the total number N_δ is a power law of δ, i.e., $N_\delta \sim \delta^{-D_\delta}$, with D_δ, the box-counting dimension of the structure, being noninteger.
[30] B. H. Kaye, *A Random Walk Through Fractal Dimensions* (VCH Publishers, New York, 1989).
[31] M. A. Soare and R. C. Picu, Int. J. Numer. Methods Eng. **74**, 668 (2008).
[32] R. G. Ghanem and P. D. Spanos, *Stochastic Finite Elements: A Spectral Approach* (Springer-Verlag, New York, 1991).
[33] C. Zener, *Elasticity and An Elasticity of Metals* (University of Chicago Press, Chicago, 1948).